Journal of Alloys and Compounds 1065 (2026) 187976

Contents lists available at ScienceDirect

Journal of Alloys and Compounds

journal homepage: www.elsevier.com/locate/jalcom

Boron-functionalized AlTiMgSi powders for *in-situ* precipitation of TiB_2 grain refiners during laser powder bed fusion

Giorgia Lupi [a], Neyder Sandoval [b], Edward W. Lui [c], Sophia Alexandra Tsipas [b], Riccardo Casati [a,*]

[a] Department of Mechanical Engineering, Politecnico di Milano, Via G. La Masa 34, Milano, MI 20156, Italy
[b] University Carlos III of Madrid, Department of Materials Science and Engineering and Chemical Engineering, IAAB, Avda. de la Universidad, 30, Leganés, Madrid 28911, Spain
[c] Centre for Additive Manufacturing, School of Engineering, RMIT University, VIC 3000, Australia

ARTICLE INFO

Keywords:
Additive manufacturing
Laser powder bed fusion
Aluminum alloys
Powder functionalization
Grain refinement
Mechanical properties

ABSTRACT

Producing Al powder feedstock containing high levels of Ti and B through gas atomization remains technologically challenging. In this study, a different route is proposed based on the functionalization of powder surfaces rather than pre-alloying. A Ti-bearing Al-Mg powder was modified by decorating its surface with 0.5 wt% of boron nanoparticles via a fluidized-bed process. This approach enabled powder surface decoration with B, leading to in-situ TiB_2 formation during Powder Bed Fusion - Laser Beam (PBF-LB/M), without the need for ex-situ ceramic additions. The approach, demonstrated here on an AlTiMgSi alloy, can be easily extended to other systems to design in-situ reinforced feedstocks for additive manufacturing. The results showed that the AlTiMgSi alloy is characterized by a partial suppression of epitaxial growth in PBF-LB/M due to the presence of Al_3Ti. In contrast, when B was added to the powder surface, the refinement effect was significantly enhanced, due to the combined effect of formation of TiB_2 particles and the segregation of excess Ti at their surface promotes the formation of Al_3Ti. After solution treatment and aging, differences in Al_3Ti precipitation behavior were observed in the two investigated systems: the B-free alloy showed a dense distribution of acicular precipitates, whereas the functionalized alloy exhibited coarser and fewer Al_3Ti particles due to Ti consumption during TiB_2 formation. The AlTiMgSi(B) alloy exhibited higher ultimate tensile strength (305.7 ± 0.2 MPa) and yield strength (273.9 ± 8.1 MPa) compared to the B-free alloy (264.6 ± 5.9 MPa and 214.1 ± 0.2 MPa, respectively).

1. Introduction

Additive manufacturing (AM) is rapidly expanding towards the production of structural and functional components. This evolution inevitably requires a broader range of materials than those currently available. However, the materials currently used for these techniques are mainly metallic systems and alloys, including titanium alloys, nickel superalloys, cobalt-chromium alloys, aluminum alloys, stainless steels, and tool steels [1,2]. These alloys, however, were originally developed for conventional manufacturing processes. As a result, a key challenge is the development of tailored alloys specifically designed to further advance AM technologies. Indeed, the processability of certain metal powder grades, such as nickel superalloys, aluminum alloys, and pure copper, can pose significant challenges due to their susceptibility to solidification and liquation cracking, or high laser-reflectivity [3–7]. For instance, Al alloys of the 2xxx series are highly prone to solidification cracking [8]. The case of high-strength Al alloys is particularly critical: most wrought compositions that display excellent mechanical properties are also among the most difficult to process, due to their marked hot-crack sensitivity [3–7,9]. Hot cracking occurs during solidification when the solid–liquid interface becomes unstable. As the temperature and liquid volume fraction decrease, volumetric solidification shrinkage and thermal contraction in these regions create cavities and hot cracks, which can potentially span multiple layers [10,11]. In this context, the addition of heterogeneous nucleation sites plays a crucial role. The addition of Ti and B, which leads to the formation of TiB_2 particles, has been shown to be an effective grain refinement strategy, significantly reducing the alloy's susceptibility to hot cracking [12]. However, producing Al powder feedstock with high amounts of Ti and B via gas atomization presents significant challenges. The high reactivity of B with

* Corresponding author.
E-mail address: riccardo.casati@polimi.it (R. Casati).

https://doi.org/10.1016/j.jallcom.2026.187976
Received 23 December 2025; Received in revised form 9 April 2026; Accepted 11 April 2026
Available online 13 April 2026

Ti in the molten bath results in the formation of borides that tend to separate from the liquid phase, causing non-homogeneous boride distribution and leading to issues such as nozzle clogging during powder production [13,14]. An alternative approach involves modifying only the surface of the powder particles. Several works have demonstrated that also the ex-situ addition of TiB_2 is effective in suppressing the formation of hot cracks by promoting grain refinement [15–17]. However, a previous work by some of the authors of this paper demonstrated that pre-alloying Ti and B into the powder is more effective than ex-situ additions in generating a refined grain structure and improving mechanical performance [18]. Therefore, developing a method that enables the exclusive formation of fine, uniformly distributed in-situ TiB_2 particles is crucial to achieving enhanced mechanical and functional properties.

In this work, a new powder functionalization strategy is explored to overcome the limitations of pre-alloying. Specifically, the surface of an AlTiMgSi powder was decorated with 0.5 wt% of B nanoparticles using a fluidized-bed process. This approach aims to demonstrate that boron can be deposited on the particle surface and effectively promote in-situ formation of TiB_2 during Powder Bed Fusion - Laser Beam (PBF-LB/M), without relying on ex-situ TiB_2 additions. Moreover, by adjusting the B content, this method offers a useful tool to enhance the processability of crack-sensitive Al alloys and to produce composite materials with tailored properties, combining high reinforcement content with optimized microstructural and mechanical performance. Although demonstrated here using an AlTiMgSi alloy as a case study, the proposed surface functionalization strategy can be readily extended to other alloy systems, offering a general and scalable route to improve the processability and performance of powders for AM.

Recent evidence demonstrated that altering the powder feedstock composition may affect multiple stages of the manufacturing route, from laser processing to post-processing treatments. In addition to influencing grain refinement during solidification, feedstock modification may modify the processing window in PBF-LB/M, but more importantly it can change the precipitation behavior during heat treatment [19]. Building on this evidence, the present work systematically investigates how surface functionalization with B nanoparticles affects process optimization, microstructural evolution, and mechanical performance in PBF-LB/M, with the aim of clarifying the broader implications of powder modification strategies.

2. Experimental and numerical methods

2.1. Powder feedstock

AlTiMgSi powder was produced by Kymera International [20] through gas atomization. The chemical composition is reported in Table 1. The particle size distribution (PSD) of the powder was as follows: particles with a diameter below 20 μm accounted for 9.5%, those between 20 μm and 63 μm represented 94.4%, while only 0.1% of the particles exceeded 63 μm.

Subsequently, the powder was functionalized by a fluidized-bed coating process, by adding 0.5 wt% of B nanoparticles uniformly onto the surface of the AlTiMgSi particles. Amorphous B nanoparticles with a nominal average particle size of 200 nm were used (see Supplementary material 1).

To achieve optimum homogeneity, the B nanoparticles were first dispersed in colloidal suspensions before their deposition onto the AlTiMgSi host powder. Distilled water was used as the dispersion medium. To optimize the stability and dispersion of the nanoparticle suspensions, the isoelectric point and zeta potential were measured using a Zetasizer Nano ZEN3500 (Malvern Instruments Ltd., Spain) as a function of the suspension pH. Suspensions containing 0.1 g/L of nanoparticles were prepared and their pH was adjusted using HNO_3 and Tetramethylammonium hydroxide (TMAH). In addition, to ensure proper nanoparticle dispersion and adhesion to the host particles, polyethylenimine (PEI) was added to the suspensions at different weight fractions relative to the nanoparticles (0.5, 1 and 2 wt%). The surface charge of the nanoparticles was evaluated, and the most stable suspension conditions were identified.

The surface modification of the AlTiMgSi powder was performed in a stainless steel fluidized bed reactor equipped with a distributor plate with an average pore size of 5 μm. The powder bed of the AlTiMgSi host powder was placed in the reactor, and 50 mL of the stable nanoparticle suspension were introduced into the fluidized bed via a spray nozzle. The amount of nanoparticles in the suspension, with respect to the total weight of the AlTiMgSi host powder, was 0.5 wt%. Prior to being sprayed, the nanoparticle suspensions were treated with an ultrasonic probe at 300 W for 1 h to ensure complete dispersion. Argon with a purity of 99.5% was used as the fluidization gas. The gas flow rate was maintained above the minimum fluidization threshold, and the pressure drop across the distributor plate was kept sufficiently high to decouple the gas supply from bubble formation within the bed. To facilitate evaporation of the suspensions during coating, the reactor was heated to 120 °C and the inlet gas was dried to remove residual moisture.

2.2. Thermo-Calc simulations

The Thermo-Calc software with the TCAL8 database was employed to investigate the effect of different alloying elements on the solidification behavior of Al alloy and to assess the influence of B. Scheil–Gulliver simulations were performed to predict the evolution of phases during non-equilibrium solidification, providing insights into the formation of reinforcing TiB_2 particles.

2.3. Printing and heat treatments

A Renishaw AM250 equipped with the Reduced Build Volume (RBV) module was used to manufacture cubic samples ($8 \times 8 \times 8$ mm^3) for density and microstructural analyses using both AlTiMgSi and AlTiMgSi (B) powders. The relative density of the printed samples was evaluated on polished cross sections parallel to the building direction using ImageJ software. Optical microscopy observations were performed with a Nikon Eclipse LV150NL light optical microscope (LOM) equipped with a 25 × objective lens. The optimal combination of printing parameters to achieve the highest density for each powder feedstock was identified and is reported in Table 2 (the optimization procedure is not detailed in this work). These optimized parameters were subsequently used to produce samples for microstructural characterization and micro-tensile testing.

Heat treatments were carried out to evaluate their effect on the microstructure and mechanical properties of both alloys. The thermal cycle consisted of a solution treatment at 530 °C for 1 h, followed by water quenching and subsequent artificial aging at 180 °C. The aging parameters were defined through a preliminary study aimed at identifying the peak hardness condition, based on Vickers microhardness

Table 1
Nominal chemical composition of the AlTiMgSi powder (wt%).

Mg	Si	Ti	Al
1.12	0.78	1.4	Balance

Table 2
Optimized process parameters used to print the samples.

	AlTiMgSi	AlTiMgSi(B)
Laser power	200 W	200 W
Time of exposure	140 μs	140 μs
Point distance	80 μm	60 μm
Hatch distance	80 μm	80 μm
Layer thickness	25 μm	25 μm

measurements performed using a Future-Tech FM-810 system. The full optimization procedure is not detailed in this work. The peak hardness condition (T6) was achieved after aging the AlTiMgSi alloy for 4 h and the AlTiMgSi(B) alloy for 2 h.

2.4. Microstructural characterization

The analysis of microstructures of bulk samples at relatively low magnification was performed by LOM and a field emission scanning electron microscope (SEM, Zeiss Sigma 500) equipped with energy dispersive X-ray analysis (EDX) and secondary electron and back-scattered electron detectors (EBSD).

X-ray diffraction (XRD) analyses were performed on bulk materials with a Rigaku SmartLab diffractometer employing Cu Kα radiation. The data were obtained in the diffraction angle range $30^\circ \leq 2\theta \leq 80^\circ$, with a step width of 0.01° and a velocity of 0.5°/min.

Transmission electron microscopy (TEM) analyses were carried out on as-built (AB) and T6 samples produced both with the AlTiMgSi and AlTiMgSi(B) powder feedstocks. Thin lamellae were prepared using a FEI Scios DualBeam FIB-SEM system. TEM observations were performed using a FEI Tecnai G2 Spirit TWIN microscope equipped with a LaB_6 electron source, operating at an acceleration voltage of up to 120 kV. The system is fitted with both an FEI Eagle 4k bottom-mounted CCD camera and an Olympus SIS MegaView G2 side-mounted CCD camera, offering a magnification range from 18 × to 650,000 × and a line-to-line resolution of 0.20 nm.

2.5. Mechanical tests

Micro-tensile tests were carried out using an MTS-Alliance RT/100 universal testing machine to evaluate the mechanical response of the materials in the as-built and heat-treated conditions. In total, six specimens were tested. For the heat-treated condition, two specimens were tested for each alloy to ensure reproducibility of the results. In contrast, only one specimen per alloy was tested in the as-built condition, as the samples exhibited pronounced brittleness. The specimens had a gauge section with a thickness of 1 mm, a width of 3 mm, and a gauge length of 6 mm. The samples were directly fabricated in their final geometry by PBF-LB/M, followed by grinding and mechanical polishing to remove surface irregularities. Due to the small dimensions of the specimens, some scatter in mechanical performance is expected, particularly affecting the strain at failure and the ultimate tensile strength (UTS).

3. Results

3.1. Powder characterization

Boron suspensions exhibited an isoelectric point at pH 4–4.5 and zeta potential values between –31 and –45 mV under alkaline conditions (pH 8–10), indicating a limited stability. In contrast, as shown in Fig. 1, the addition of PEI significantly modified the electrostatic behavior of the suspensions. The isoelectric point shifted to approximately pH 10, and the zeta potential became consistently positive across a broad pH range (2–8), reaching values between + 40 and + 70 mV depending on the PEI concentration. This behavior confirms that PEI effectively reverses the particle surface charge and enhances colloidal stability. When PEI is dissolved under basic conditions, the nanoparticle surfaces adsorb ionized PEI molecules, becoming positively charged and exhibiting a full reversal of the original negative surface potential [21].

Among the tested formulations, suspensions prepared with 2 wt% PEI and adjusted to near-neutral pH displayed the most favorable characteristics, achieving zeta potentials of + 50 to + 60 mV. These values meet the widely accepted criteria for colloidal stability, in which zeta potentials above ±30 mV indicate stable suspensions, while values exceeding ±60 mV denote excellent stability [22–24]. Therefore, B suspensions containing 2 wt% PEI were selected for nanoparticle deposition onto the AlTiMgSi powder in the fluidized-bed reactor.

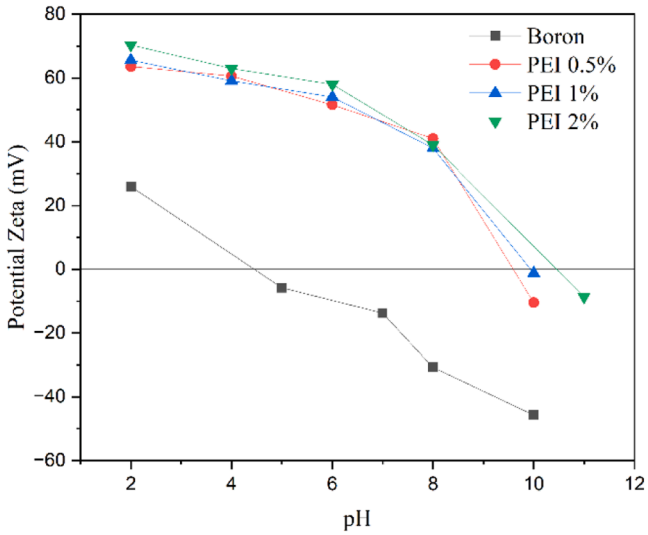

Fig. 1. Variation of Zeta Potential of colloidal suspension of boron with different percentages of PEI.

Fig. 2 presents SEM images of the powder feedstocks before and after the surface functionalization process. The AlTiMgSi powder (Fig. 2a) exhibits the typical morphology expected from gas-atomized powders. High-magnification SEM observations (Fig. 2c) allowed for the identification of boron nanoparticles (see Supplementary material 1), meaning that the fluidized-bed process proved effective in decorating the surface of the Al powder.

3.2. Thermo-Calc simulations

Thermo-Calc simulations were carried out to predict the solidification sequence of the investigated alloys using the Scheil–Gulliver solidification model. The resulting phase evolution as a function of temperature is reported in Fig. 3. In the B-free alloy, the first intermetallic phase predicted to form is Al_3Ti. Conversely, in the B-containing alloy, TiB_2 is predicted to nucleate first, preceding the formation of Al_3Ti. B addition alters the solidification pathway, promoting the early formation of stable TiB_2 particles that can act as effective heterogeneous nucleation sites for α-Al.

3.3. Characterization of as-built materials

Following the optimization of process parameters, bulk samples were successfully printed and characterized to evaluate their microstructures and mechanical properties. The density analysis of bulk samples was conducted by examining the cross sections, both normal and parallel to the z-axis, of three cubes following the ASTM F3637 −23 standard [25]. Image analysis was performed with ImageJ to evaluate the relative density of the samples, which was found to be 99.8% and 99.4% for the AlTiMgSi and AlTiMgSi(B) powders, respectively.

Fig. 4 compares the microstructures of the investigated alloys. The B-free alloy is characterized by a mixed grain morphology with both equiaxed and elongated grains. EBSD and SEM analyses show finer grains near the melt-pool boundaries, where a high density of bright particles is observed. Their strong contrast with the darker matrix indicates Ti enrichment, suggesting that they are primary Al_3Ti particles, consistent with Scheil simulation results. In contrast, the addition of B nanoparticles to the powder surface led to a fully equiaxed microstructure with an average grain size below 1 μm, and the typical melt-pool morphology was no longer visible. The functionalization of the feedstock with B effectively enhances the heterogeneous nucleation of α-Al phase in the printed material (Fig. 4 f), thereby suppressing the epitaxial

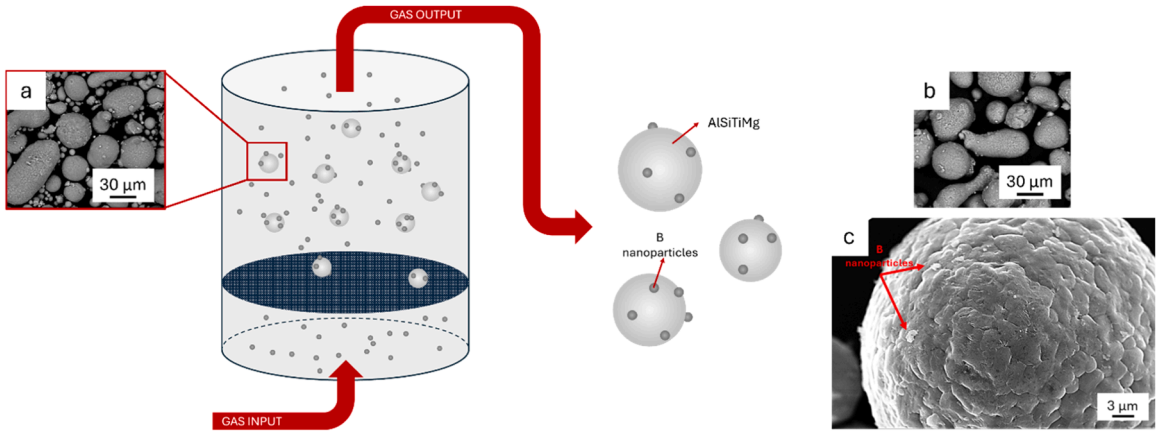

Fig. 2. SEM micrographs of the powder feedstock. a) AlTiMgSi powder and b),c) powder feedstock after surface functionalization where the red arrows indicate B nanoparticles.

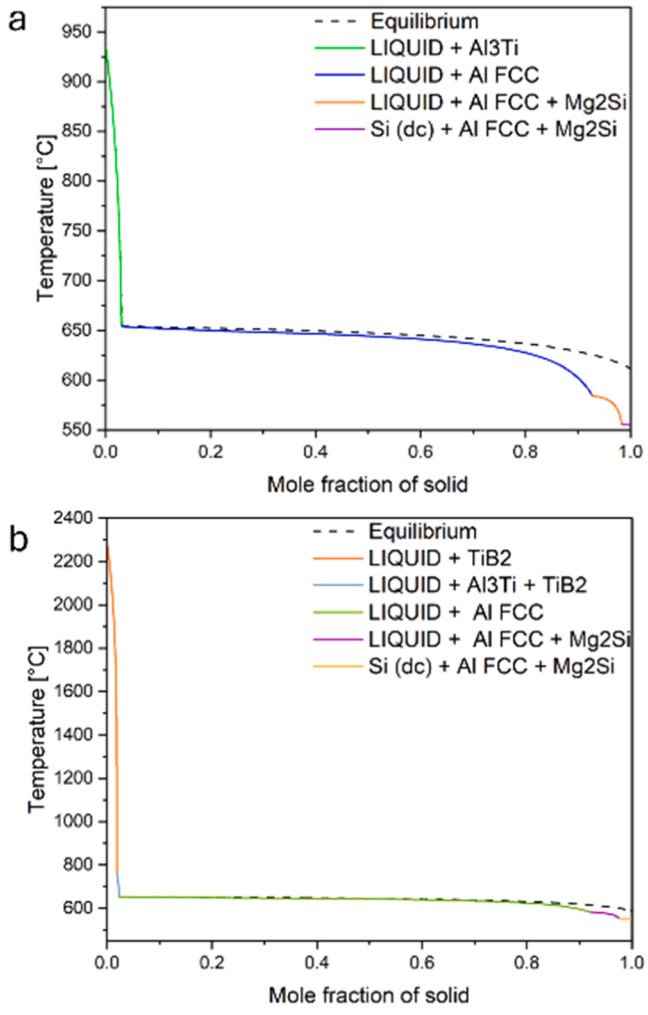

Fig. 3. Scheil-Gulliver solidification curve of a) AlTiMgSi alloy and b) AlTiMgSi (B) alloy.

growth of columnar grains from previously deposited layers [26]. A more homogeneous distribution of bright particles is also observed, likely corresponding to TiB_2 and Al_3Ti. However, SEM alone does not allow unambiguous phase identification and for this reason TEM analyses were performed on both AlTiMgSi and AlTiMgSi(B) alloys in as-built condition (Fig. 5). In the B-free alloy, TEM images clearly revealed elongated grains, consistent with the epitaxial growth observed by EBSD. Selected area electron diffraction (SAED) patterns acquired at grain boundaries exhibited diffraction spots corresponding to Al_3Ti phase in the tetragonal $D0_{22}$ structure. (Fig. 5b). In AlTiMgSi(B), TiB_2 precipitates are present both within the grains and at the grain boundaries. SAED analysis performed at the grain boundaries revealed diffraction spots corresponding to both $D0_{22}$- Al_3Ti and TiB_2 phases (Fig. 5e). Fig. 5 f reports TEM image of a TiB_2 particles, its SAED pattern exhibited faint hexagonally arranged streaks around the main diffraction rings. These hexagonal streaks are typically observed in crystals with hexagonal symmetry (in the present case TiB_2) and originate from the overlap of reflections from parallel crystallographic planes with similar interplanar spacings but different angular orientations. In such cases, the planes produce constructive interference along specific directions, resulting in the characteristic streaked pattern observed in the diffraction image [27,28].

3.4. *Characterization of the heat-treated materials*

The microstructure of the alloys in the heat-treated condition was first examined via SEM, and the results are shown in Fig. 6. In both AlTiMgSi and AlTiMgSi(B) alloys, the T6 heat treatments promoted the formation of finely dispersed nanometric precipitates throughout the matrix. No evident morphological differences between the two alloys were observed through the SEM analysis. However, the small size of these precipitates makes them challenging to characterize reliably using SEM and EDX. To gain a more detailed understanding of the precipitate characteristics, including size and distribution, TEM analyses were performed on T6 samples. The results are reported in Fig. 7. In the AlTiMgSi alloy (Fig. 7a and b), TEM images show the presence of homogeneously dispersed rod-like thin precipitates, which were identified as $D0_{22}$- Al_3Ti by SAED. In the AlTiMgSi(B) alloy, the density of $D0_{22}$- Al_3Ti precipitates is lower. Nonetheless, $D0_{22}$- Al_3Ti precipitates are still present in this alloy, appearing bulkier compared to the thin acicular ones in the B-free alloy (Fig. 7c and d). The TEM images also confirm the presence of TiB_2 nanoparticles, highlighting their stability after exposure to elevated temperatures (Fig. 7d). Additionally, both alloys exhibit Mg_2Si precipitates, which appear as polyhedral or cubic particles (Fig. 7e and f).

To further support phase identification, XRD analyses were performed on both AlTiMgSi and AlTiMgSi(B) alloys in the as-built and T6 heat-treated conditions. The corresponding diffraction patterns are reported in Fig. 8. In both alloys, the dominant reflections arise from the α-Al matrix. In addition, diffraction peaks attributable to Al_3Ti were detected, and their positions are consistent with the tetragonal $D0_{22}$ structure. In the heat-treated conditions, reflections attributable to

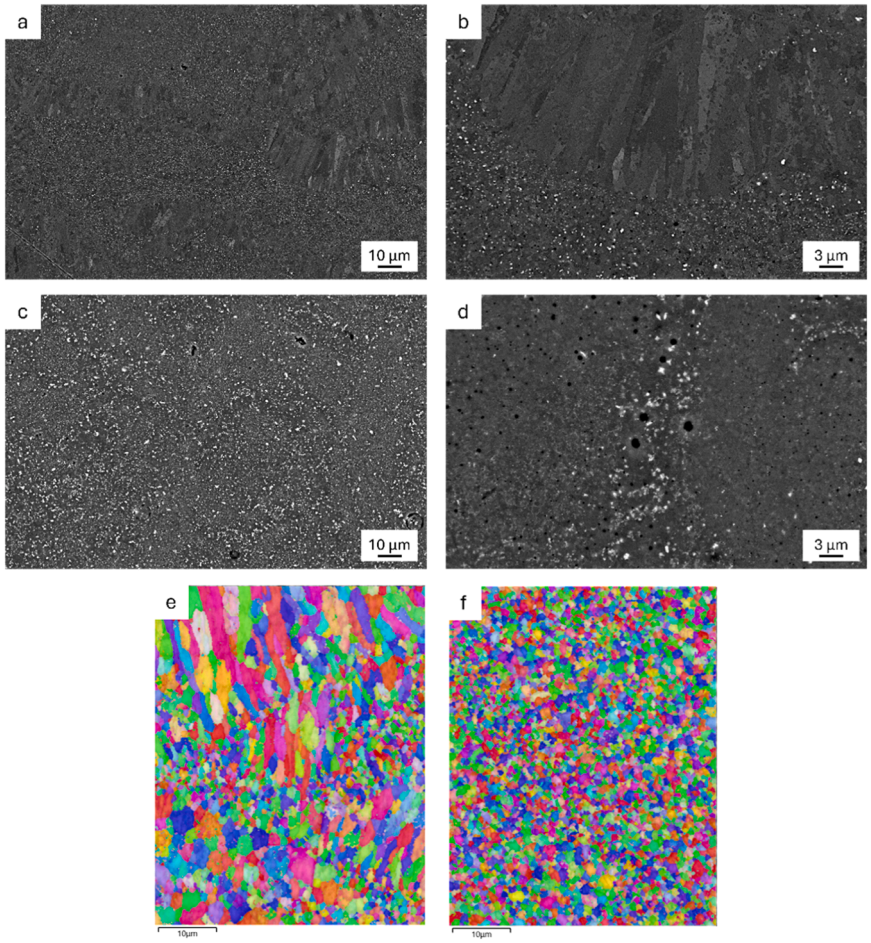

Fig. 4. a), b) SEM images and e) IPF map of the AlTiMgSi alloy. c), d) SEM images and f) IPF map of the AlTiMgSi(B).

Mg_2Si were also observed, in agreement with the TEM observations of Mg_2Si precipitates after T6 treatment. In the AlTiMgSi(B) alloy no distinct TiB_2 reflections were resolved in the XRD patterns, likely to its low volume fraction and fine particle size, which limit detectability by XRD.

Tensile tests were performed on the materials in as-built (AB) and heat-treated (T6) conditions, and the curves are presented in Fig. 9. The AlTiMgSi(B) alloy exhibited a higher ultimate tensile strength (UTS) (257.2 MPa in AB and 305.7 MPa in T6) and yield strength (YS) (236.3 MPa in AB and 273.9 MPa in T6) compared to the AlTiMgSi alloy. This improvement confirms the strengthening effect of TiB_2 nanoparticles.

Moreover, it is worth mentioning that the adopted specimen geometry reproduces a thin-wall structure, with a final thickness below 1 mm. Such a reduced cross-section strongly amplifies the influence of defects and surface imperfections on the overall mechanical response. Therefore, the obtained results should be regarded as preliminary indicators of the mechanical behavior of the alloy and represent a lower bound of the expected properties for fully dense bulk samples.

4. Discussion

The fluidization process enabled uniform and homogeneous deposition of B nanoparticles onto the AlTiMgSi powder. Continuous particle–nanoparticle interactions within the fluidized bed facilitated consistent surface coverage, confirming the effectiveness of this method for the surface functionalization of metallic powders. The B nanoparticles appear homogeneously dispersed onto the powder surface, with no evidence of large agglomerates (Fig. 2). This homogeneous distribution is particularly important, as it ensures uniform energy absorption during laser processing and promotes homogeneous in-situ formation of TiB_2 in the bulk material. Moreover, after the functionalization treatment, the particles retained their spherical shape, confirming that the process did not alter the original morphology of the feedstock. The spherical morphology is crucial for ensuring good flowability and processability in the subsequent printing step.

Fully dense cubic samples were successfully printed using PBF-LB/M with both powder feedstocks. The microstructure of the AlTiMgSi alloy highlights that the presence of Al_3Ti only partially suppresses epitaxial growth, resulting in a duplex grain morphology (Fig. 4e), composed of both equiaxed and elongated grains. The equiaxed grains are mainly concentrated at the melt pool boundaries, where SEM observations reveal a high density of fine precipitates (Fig. 4b). These particles are too small to be precisely identified by EDX, but their bright contrast indicates that they are Ti-rich, likely Al_3Ti as predicted by Scheil simulations. TEM analysis confirmed the presence of elongated grains (Fig. 5a) while XRD analysis and SAED patterns acquired at grain boundaries consistently displayed diffraction spots of $D0_{22}$- Al_3Ti (Fig. 5b and Fig. 8). In this case, grain refinement can be primarily attributed to the peritectic theory [29,30]. During cooling, Ti-rich particles such as Al_3Ti act as stable substrates for the heterogeneous nucleation of α-Al. According to the peritectic model, the interfacial reaction between the remaining liquid and pre-existing Al_3Ti promotes the formation of a thin α-Al layer at the particle surface, enhancing nucleation without requiring significant undercooling. This mechanism has been widely reported as a key factor governing grain refinement in Al-Ti systems [31]. In addition to the peritectic nucleation mechanism, the observed enrichment of Al_3Ti at grain boundaries suggests that grain refinement

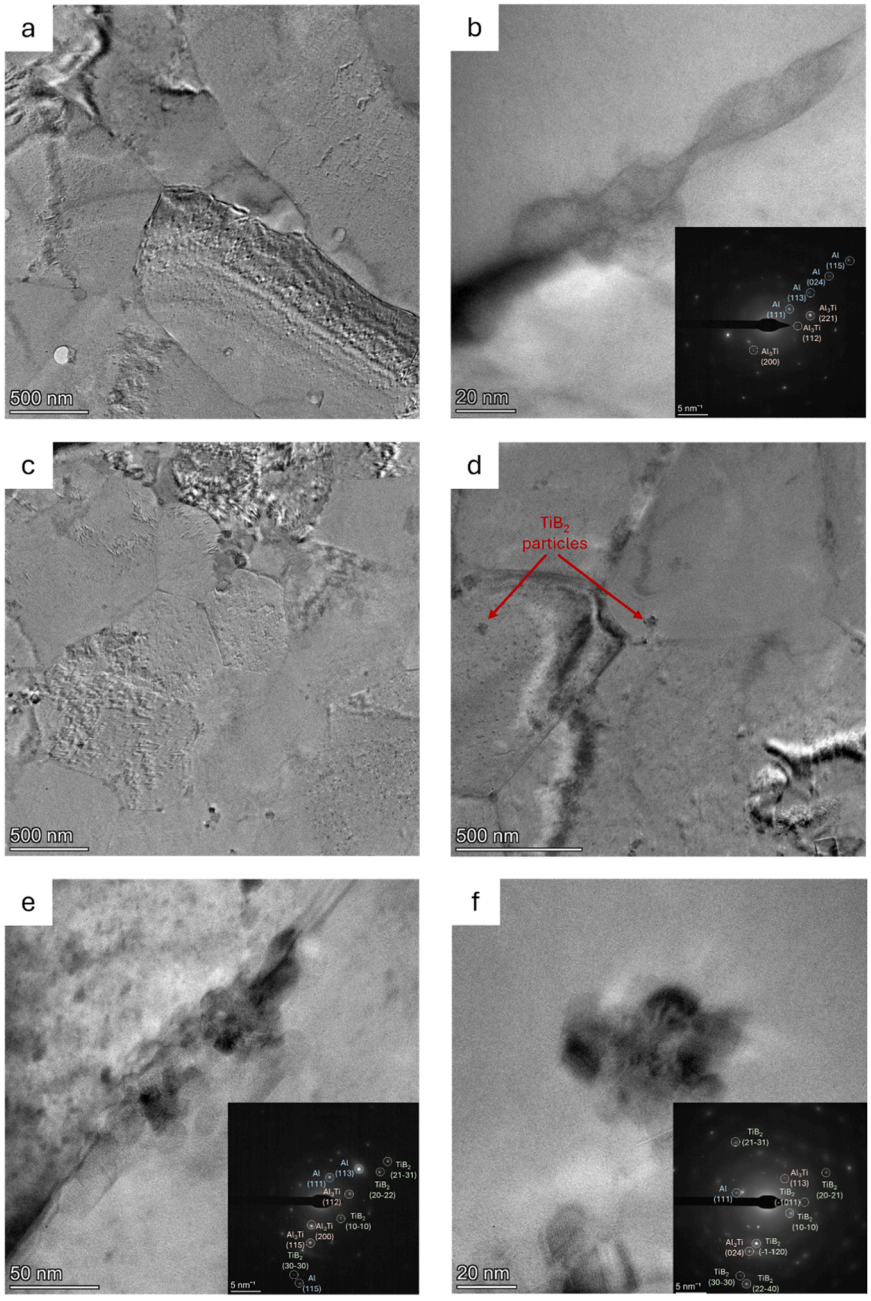

Fig. 5. a),b) TEM images of the AlTiMgSialloy in as-built condition; the corresponding SAED pattern for image b) is shown. c), d, e), f))TEM images of the AlTiMgSi (B) alloy in as-built condition; the corresponding SAED patterns for images e) and f) are shown.

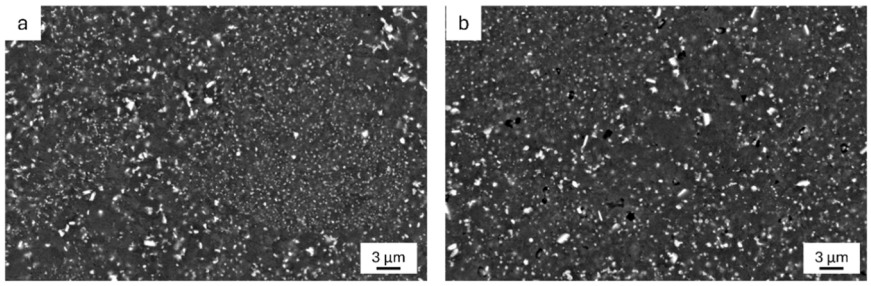

Fig. 6. SEM images of the a) AlTiMgSi and b) AlTiMgSi(B) alloys in T6 condition.

may also be influenced by solute segregation effects. During solidification, dissolved Ti can segregate ahead of the solid–liquid interface, increasing the local solute content in the melt and generating constitutional supercooling. This solute-induced undercooling restricts the

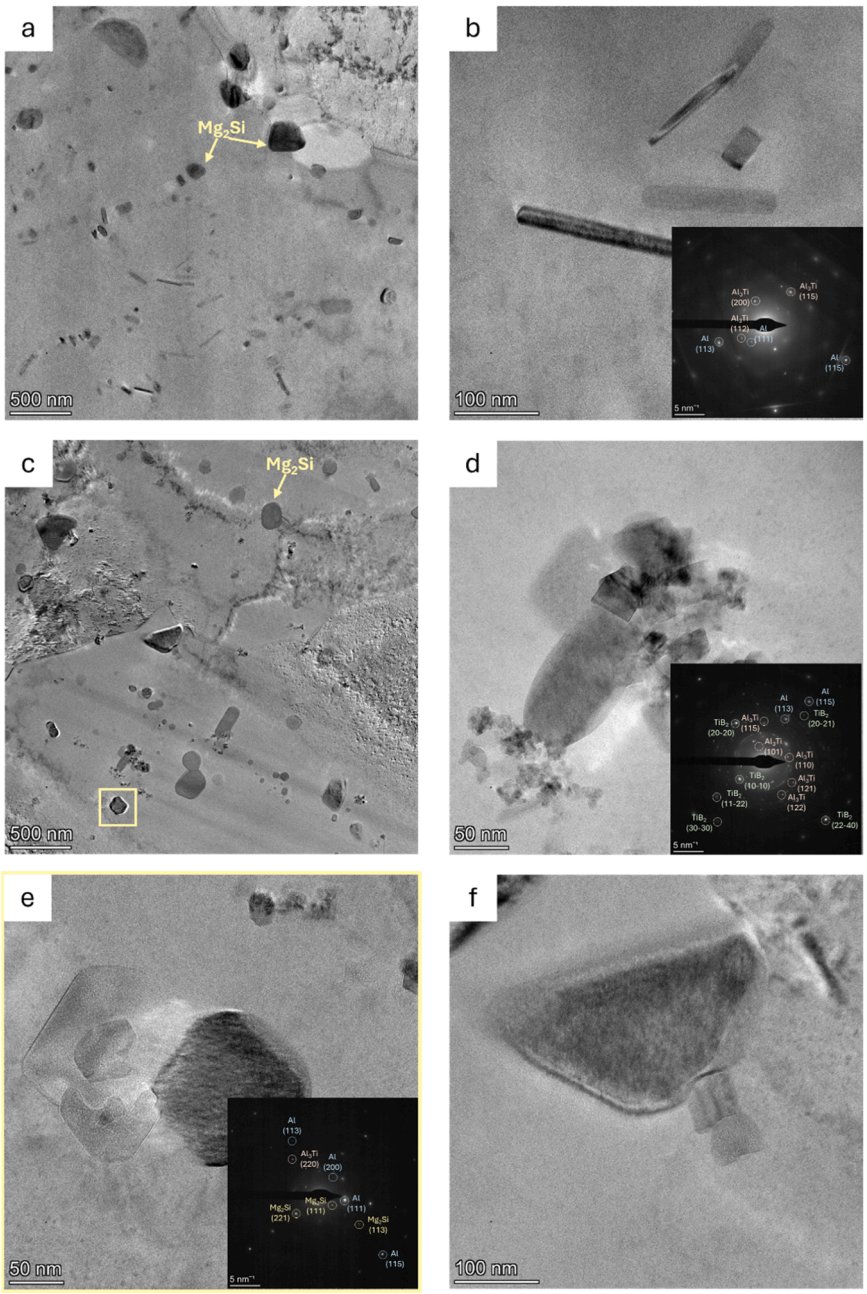

Fig. 7. a), b) TEM images of the AlTiMgSi alloys in T6 condition; the corresponding SAED pattern for image b) is shown. c), d), TEM images AlTiMgSi(B) in T6 condition; the corresponding SAED pattern for image d) is shown. e), f) TEM images of Mg_2Si precipitates.

growth of existing grains and enhances the driving force for the nucleation of new α-Al grains [32,33]. The duplex grain microstructure and the inhomogeneous precipitate distribution can be explained by variations in the solidification front velocity across the melt pool. As the solidification front velocity increases toward the melt pool top region, approaching the beam scanning velocity, solute trapping becomes significant [34]. Under these high solidification velocities, the formation of primary Al_3Ti can be locally suppressed, causing Ti to remain in supersaturated solid solution within the columnar α-Al grains rather than forming Al_3Ti particles [35,36].

A markedly different behavior is observed when B is added to the powder surface. Indeed, in this case the refinement effect was significantly enhanced, and the heterogeneous nucleation of the α-Al phase occurred more uniformly. As a result, the columnar-to-equiaxed grain transition (CET) was complete, leading to an average grain size below 1 μm (Fig. 4c and Fig. 4 f). TEM micrographs (Fig. 5c and Fig. 5d) further confirmed the presence of a fully refined grain structure, with local grain sizes down to approximately 500 nm. In the B-containing alloy, the refinement mechanism can be explained by the duplex nucleation and solute growth restriction theories [37]. In this case, TiB_2 particles serve as stable substrates for heterogeneous nucleation, while Ti segregates at their surface, forming a thin Al_3Ti layer. It has been reported that TiB_2 particles alone are not effective nucleation sites for α-Al grains in liquid aluminum, rather, the presence of solute Ti modifies the interfacial structure and growth kinetics, leading to the formation of an efficient TiB_2/ Al_3Ti nucleating interface [38,39]. The synergy between TiB_2 and Al_3Ti has been demonstrated to be a powerful grain-refinement mechanism. Since α-Al requires a lower undercooling in the presence of Al_3Ti than TiB_2, Al_3Ti is generally considered the effective nucleant in such systems [40]. Thermo-Calc simulations (Fig. 3b) support these

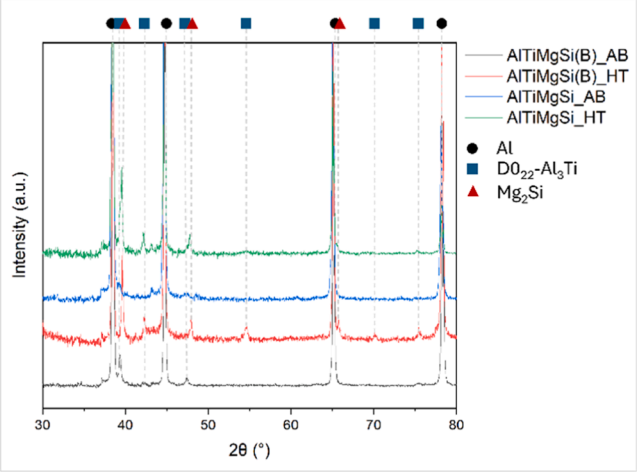

Fig. 8. XRD patterns of the AlTiMgSi and AlTiMgSi(B) alloys in as-built and T6 conditions.

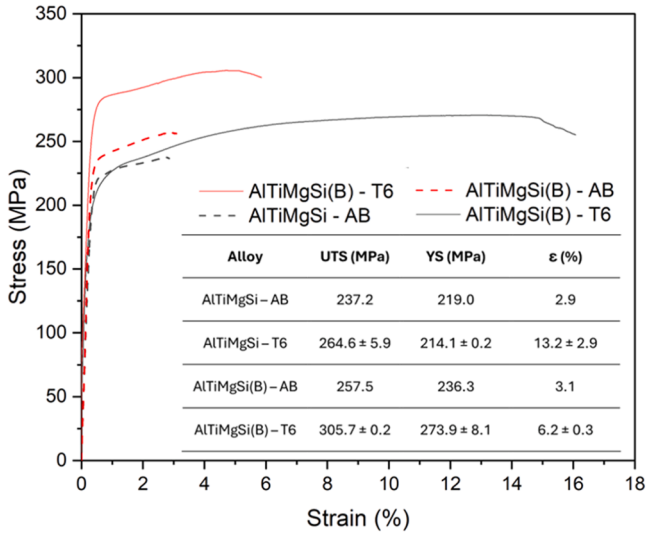

Alloy	UTS (MPa)	YS (MPa)	ε (%)
AlTiMgSi – AB	237.2	219.0	2.9
AlTiMgSi – T6	264.6 ± 5.9	214.1 ± 0.2	13.2 ± 2.9
AlTiMgSi(B) – AB	257.5	236.3	3.1
AlTiMgSi(B) – T6	305.7 ± 0.2	273.9 ± 8.1	6.2 ± 0.3

Fig. 9. Stress vs strain curves of the AlTiMgSi and AlTiMgSi(B) alloys in as-built and T6 conditions.

interpretations, predicting the initial formation of TiB_2 followed by Al_3Ti. Additionally, as mentioned above, the presence of solute Ti in the melt promotes constitutional undercooling ahead of the solidification front, restricting grain growth and further contributing to the development of a fine equiaxed grain structure [41].

Importantly, while previous work using high-resolution TEM has directly observed a continuous Al_3Ti layer at TiB_2 interfaces [40,42], such a layer was not observed in this study, because of the limited spatial resolution of the TEM analysis employed here, which may prevent the detection of extremely thin interfacial layers. SAED patterns acquired in regions containing TiB_2 particles consistently revealed diffraction spots attributable to Al_3Ti, indicating the coexistence of Al_3Ti and TiB_2 in the analysed areas. Although these observations do not provide direct interfacial proof of a duplex TiB_2/Al_3Ti nucleation structure, they are consistent with the mechanism proposed in the literature and suggest that a similar grain-refinement mechanism may operate in the present alloy.

During the subsequent T6 heat treatment, both alloys exhibited Mg_2Si precipitates with polyhedral or cubic morphology (Fig. 7 and Fig. 8). In Al-Si-Mg alloys subjected to T6, the precipitation pathway typically involves the formation of the β" (needle-shape) and β' (rod-shape) metastable phases before the appearance of the equilibrium β (Mg_2Si) phase. β″ is usually the dominant precipitate in the peak-aged condition [43,44]. Some studies have reported that the addition of Ti can inhibit or delay the formation of these Mg–Si metastable precipitates, since Ti-rich intermetallics can capture Si and compete with the nucleation of the β" and β' phases [19,45]. In the present alloys, however, coarse Mg_2Si precipitates are clearly observed after T6, and their presence is also consistent with the XRD results (Fig. 8). Examination of the micrographs (Fig. 7e and Fig. 7 f) suggests that some Mg_2Si particles may nucleate on, or grow in contact with pre-existing rod--shaped particles, resembling Al_3Ti. While their morphology is compatible with Al_3Ti, the available SAED data do not allow their unambiguous identification.

The evolution of Ti-containing precipitates during T6 differed markedly between the two alloys and highlights a key implication of powder functionalisation: modifying the feedstock composition affects not only grain refinement during PBF-LB/M, but also the subsequent precipitation response during heat treatment. The evolution of Ti-containing precipitates upon T6 heat-treatments is important since they are known to contribute to alloy strengthening [46]. Comparison between the as built and heat-treated microstructures strongly suggests that a significant fraction of the fine Ti containing particles observed after T6 formed during heat treatment (Fig. 6).

In the B-free alloy (Fig. 7a), Ti is not consumed by TiB_2 formation during solidification and therefore remains available in solid solution to a greater extent than in the B-bearing alloy. This condition promotes the nucleation of a larger number of Al_3Ti precipitates throughout the matrix during aging, resulting in a denser dispersion of fine particles. Conversely, in the B-containing alloy (Fig. 7c), the reduced availability of Ti in solid solution limits the formation of Al_3Ti precipitates. In addition, Ti-rich precipitates tend to form heterogeneously on retained TiB_2 particles, leading to coarser features compared to the finer Al_3Ti precipitates that form homogeneously from a highly supersaturated α-Al solid solution.

These findings further demonstrate that modifying the powder feedstock is not a neutral choice. Such compositional changes influence not only the grain refinement mechanism, but also the precipitation behavior during post-processing. This is particularly important from a practical standpoint, because once the alloy chemistry is modified, conventional heat-treatment parameters optimized for the base alloy may no longer be fully suitable. Therefore, dedicated alloy/heat-treatment design may be required to fully exploit the potential of the modified composition.

In line with these microstructural differences, the B-containing alloy exhibits higher strength already in the as-built state (UTS = 257.5 MPa, YS = 236.3 MPa) compared to the B-free alloy (UTS = 237.2 MPa, YS = 219 MPa). The finer grain size observed in AlTiMgSi(B) contributes to this strengthening, as the increased grain boundary density effectively impedes dislocation motion, thereby enhancing both YS and UTS. Nevertheless, the as-built ductility remains limited, with elongation to failure close to 3% for both alloys. Such low elongation is typical of PBF-LB/M processed materials and can be primarily attributed to the high level of residual stresses generated by the repeated and steep thermal cycles during processing [47,48].

After T6 heat treatment, the strengthening effect of TiB_2 becomes even more pronounced. The AlTiMgSi(B) alloy reaches UTS of 305.7 MPa and YS of 273.9 MPa, whereas the B free alloy attains only UTS of 264.6 MPa and YS of 214.1 ± 0.2 MPa. Regarding ductility, heat treatment is overall beneficial compared with the as-built state. Elongation increases from about 3.1% to 6.2 in AlTiMgSi(B), and from 2.9% to 13.2 in the B free alloy. The improvement is consistent with stress relief and the substantial modification of the characteristic PBF-LB/M cellular structure toward a coarser microstructure upon T6 heat treatment [19,49,50]. However, the B containing alloy remains less ductile than the B free alloy after T6. This reduced strain to failure can be attributed to the intrinsic tradeoff between strength and ductility in

strengthened microstructures, as commonly observed in materials with ultrafine-grained microstructures [51].

5. Concluding remarks

The fluidized-bed surface functionalization approach developed in this work successfully introduced B onto the surface of AlTiMgSi powders, enabling the in-situ TiB_2 formation during PBF-LB/M process. The combined presence of TiB_2 and Al_3Ti phases proved crucial in controlling the solidification microstructure. While Al_3Ti alone was insufficient to completely suppress epitaxial grain growth, the coexistence of TiB_2 and Al_3Ti promoted the formation of a fully equiaxed microstructure, leading to a marked improvement in both yield and ultimate tensile strength. Upon T6 heat treatment, distinct differences in Al_3Ti precipitation behavior were observed between the two alloys. The B-free alloy exhibited a dense distribution of fine acicular precipitates, whereas the functionalized alloy contained fewer and coarser Al_3Ti particles, consistent with Ti consumption during TiB_2 formation.

Overall, these findings demonstrate that the proposed powder surface functionalization strategy provides an effective and scalable strategy to tailor solidification dynamics and strengthen Al alloys processed by PBF-LB/M. The methodology is versatile and can be extended to other Ti-containing Al systems, as the amount of B introduced onto the powder surface can be precisely adjusted to achieve the desired balance between grain size, strength, and ductility. This tunability makes the approach particularly promising for optimizing both processability and performance in additively manufactured Al components, while mitigating the challenges associated with gas atomization of Ti- and B-rich feedstocks. Nevertheless, altering the powder composition also implies that processing parameters, post-processing treatments, and conventional heat-treatment schedules may need to be re-optimized to fully exploit the benefits of the modified feedstock.

CRediT authorship contribution statement

Sophia Alexandra Tsipas: Writing – review & editing, Supervision, Methodology, Investigation. **Riccardo Casati:** Writing – review & editing, Supervision, Resources, Project administration, Methodology, Formal analysis, Conceptualization. **Giorgia Lupi:** Writing – original draft, Methodology, Investigation, Formal analysis, Conceptualization. **Neyder Sandoval:** Writing – review & editing, Methodology, Formal analysis. **Edward W. Lui:** Writing – review & editing, Methodology, Investigation.

Declaration of Competing Interest

The authors declare that they have no known competing financial interests or personal relationships that could have appeared to influence the work reported in this paper.

Acknowledgments

The authors gratefully acknowledge the support of the ISIS@MACH ITALIA Research Infrastructure, the hub of ISIS Neutron and Muon Source (UK), [MUR official registry U. 0008642.28–05–2020 –16th April 2020]. IM@IT is listed in the Italian Ministry of University and Research's Piano Nazionale delle Infrastrutture di Ricerca (PNIR 2021–2027) "in the broader notion of ISIS", and ISIS Facility and IM@IT are jointly listed in high priority RI's (see Table 6 page 30, note 38, PNIR in 2021–2027). The authors would like to thank the funding provided for this research through the felllowship PIPF-2022/ECO-24706 by Comunidad de Madrid, the project TED2021–129895B-I00 by the Agencia Estatal de Ivestigacion (AEI) and the Ministerio de Ciencia, Innovación y Universidades and "Convocatoria de la Universidad Carlos III de Madrid de Ayudas para la recualificación del sistema universitario español para 2021–2023, de 1 de julio de 2021".

Appendix A. Supporting information

Supplementary data associated with this article can be found in the online version at doi:10.1016/j.jallcom.2026.187976.

References

[1] M. Schmidt, M. Merklein, D. Bourell, D. Dimitrov, T. Hausotte, K. Wegener, et al., Laser based additive manufacturing in industry and academia, CIRP Ann. 66 (2017) 561–583, https://doi.org/10.1016/J.CIRP.2017.05.011.
[2] S. Chowdhury, N. Yadaiah, C. Prakash, S. Ramakrishna, S. Dixit, L.R. Gupta, et al., Laser powder bed fusion: a state-of-the-art review of the technology, materials, properties & defects, and numerical modelling, J. Mater. Res. Technol. 20 (2022) 2109–2172, https://doi.org/10.1016/J.JMRT.2022.07.121.
[3] M.S. Kenevisi, Y. Yu, F. Lin, A review on additive manufacturing of Al–Cu (2xxx) aluminium alloys, processes and defects 37 (2021) 805–829, https://doi.org/10.1080/02670836.2021.1958487. ⟨Https://DoiOrg/101080/0267083620211958487⟩.
[4] T. Fedina, F. Belelli, G. Lupi, B. Brandau, R. Casati, R. Berneth, et al., Influence of AlSi10Mg powder aging on the material degradation and its processing in laser powder bed fusion, Powder Technol. 412 (2022) 118024, https://doi.org/10.1016/J.POWTEC.2022.118024.
[5] C. Pleass, S. Jothi, Influence of powder characteristics and additive manufacturing process parameters on the microstructure and mechanical behaviour of Inconel 625 fabricated by selective laser melting, Addit. Manuf. 24 (2018) 419–431, https://doi.org/10.1016/J.ADDMA.2018.09.023.
[6] K. Geng, Y. Yang, S. Li, R.D.K. Misra, Q. Zhu, Enabling high-performance 3D printing of Al powder by decorating with high laser absorbing Co phase, Addit. Manuf. 32 (2020) 101012, https://doi.org/10.1016/J.ADDMA.2019.101012.
[7] T. Romano, A. Ratkus, S. Gruber, M. Pozzi, H. Kos, C. Garion, et al., Pure copper membranes manufactured by green laser powder bed fusion with varying wall-thickness and building orientation: microstructure, properties, and vacuum tightness performance, Vacuum 233 (2025) 113995, https://doi.org/10.1016/J.VACUUM.2024.113995.
[8] Q. Jiang, P. Zhang, Z. Yu, H. Shi, D. Wu, H. Yan, et al., A review on additive manufacturing of pure copper, 2021, Vol 11, Page 740, Coatings 11 (2021) 740, https://doi.org/10.3390/COATINGS11060740.
[9] Belelli F., Casati R., Vedani M. Development of Al-Cu-Mg and Al-Mg-Si-Zr alloys with improved L-PBF processability, 2022, p. 289–297. https://doi.org/10.1007/978-3-030-92381-5_26.
[10] M. Schuster, A. De Luca, R. Widmer, X. Maeder, C. Leinenbach, Processability, microstructure and precipitation of a Zr-modified 2618 aluminium alloy fabricated by laser powder bed fusion, J. Alloy. Compd. 913 (2022) 165346, https://doi.org/10.1016/J.JALLCOM.2022.165346.
[11] J.H. Martin, D. Yahata, J.M. Hundley, J.A. Mayer, T.A. Schaedler, T.M. Pollock, 3D Printing of High-strength Aluminium Alloys, Nature Publishing Group, 2017, https://doi.org/10.1038/nature23894.
[12] F. Belelli, R. Casati, F. Larini, M. Riccio, M. Vedani, Investigation on two Ti–B-reinforced Al alloys for laser powder bed fusion, Mater. Sci. Eng. A 808 (2021) 140944, https://doi.org/10.1016/J.MSEA.2021.140944.
[13] A. ÜNal, Production of rapidly solidified aluminium alloy powders by gas atomisation and their applications, Powder Metall. 33 (1990) 53–64, https://doi.org/10.1179/POM.1990.33.1.53.
[14] L. Lu, M.O. Lai, H.Y. Wang, Synthesis of titanium diboride TiB2 and Ti-Al-B metal matrix composites, J. Mater. Sci. 35 (2000) 241–248, https://doi.org/10.1023/A:1004789910279/METRICS.
[15] M.X. Zhang, P.M. Kelly, M.A. Easton, J.A. Taylor, Crystallographic study of grain refinement in aluminum alloys using the edge-to-edge matching model, Acta Mater. 53 (2005) 1427–1438, https://doi.org/10.1016/J.ACTAMAT.2004.11.037.
[16] X. Li, G. Li, M.X. Zhang, Q. Zhu, Novel approach to additively manufacture high-strength Al alloys by laser powder bed fusion through addition of hybrid grain refiners, Addit. Manuf. 48 (2021) 102400, https://doi.org/10.1016/J.ADDMA.2021.102400.
[17] A. Durga, N.H. Pettersson, S.B.A. Malladi, Z. Chen, S. Guo, L. Nyborg, et al., Grain refinement in additively manufactured ferritic stainless steel by in situ inoculation using pre-alloyed powder, Scr. Mater. 194 (2021) 113690, https://doi.org/10.1016/J.SCRIPTAMAT.2020.113690.
[18] G. Lupi, L. Mariotti, A. Mistrini, J. Larsson, L. Patriarca, R. Casati, Microstructure and tensile properties of TIB2-reinforced Al-2618 thin walls produced by laser powder bed fusion, Mater. Charact. 228 (2025) 115372, https://doi.org/10.1016/j.matchar.2025.115372.
[19] G. Lupi, L. Mariotti, S. Lu, W. Xu, L. Patriarca, R. Casati, Unforeseen precipitation sequences in ex-situ/in-situ TiB2-reinforced Al2618 composites manufactured by laser-based powder bed fusion, Materials Science Engineering A 950 (2026) 149500, https://doi.org/10.1016/J.MSEA.2025.149500.
[20] Kymera International 2025. ⟨https://www.kymerainternational.com/⟩.
[21] L.-M. WANG, W.-C. WEI, Colloidal processing and liquid-phase sintering of SiC, J. Ceram. Soc. Jpn. 103 (1995) 434–443, https://doi.org/10.2109/JCERSJ.103.434.
[22] S.P. Shinde, C.B. Lobo, H.S.S. Rajput, G.F. Nikam, Nanotechnology in drug delivery system: a new approach, J. Drug Deliv. Ther. 15 (2025) 112–123, https://doi.org/10.22270/JDDT.V15I2.6988.
[23] Y. Ramaye, M. Dabrio, G. Roebben, V. Kestens, Development and validation of optical methods for zeta potential determination of silica and polystyrene particles

in aqueous suspensions, 2021, Vol 14, Page 290, Materials 14 (2021) 290, https://doi.org/10.3390/MA14020290.
[24] N.S. Kulkarni, N.S. Ranpise, D.S. Rathore, S.N. Dhole, Characterization of self-microemulsifying dosage form: special emphasis on zeta potential measurement, Int J. Pharm. Biol. Arch. 10 (2019) 172–179, https://doi.org/10.22377/IJPBA.V10I03.1809.
[25] ASTM F3637−23. Standard guide for additive manufacturing of metal — finished part properties — methods for relative density measurement. ASTM International 2023.
[26] G.K. Sigworth, T.A. Kuhn, Grain refinement of aluminum casting alloys, Int. J. Met. /Fall 7 (2007).
[27] V. Sousa, B.F. Gonçalves, M. Franco, Y. Ziouani, N. González-Ballesteros, M. Fátima Cerqueira, et al., Superstructural ordering in hexagonal CuInSe2 nanoparticles, Chem. Mater. 31 (2019) 260–267, https://doi.org/10.1021/ACS.CHEMMATER.8B04368.
[28] B. Bartova, D. Schryvers, N. Wiese, J.N. ChapmanPrecipitates and magnetic domains in an annealed Co38Ni33Al29 shape memory alloy studied by TEM. In: Proceedings of the EMC 2008 14th European Microscopy Congress 1–5 September 2008, Aachen, Germany 2008:391–392. https://doi.org/10.1007/978-3-540-85226-1_196.2008.
[29] F.A. Crossley, L.F. Mondolfo, Mechanism of grain refinement in aluminum alloys, 1951 3:12, JOM 3 (2017) 1143–1148, https://doi.org/10.1007/BF03397424.
[30] M. Easton, D. StJohn, Grain refinement of aluminum alloys: Part II. Confirmation of, and a mechanism for, the solute paradigm, Met. Mater. Trans. A Phys. Met. Mater. Sci. 30 (1999) 1625–1633, https://doi.org/10.1007/S11661-999-0099-4/METRICS.
[31] P.S. Mohanty, J.E. Gruzleski, Mechanism of grain refinement in aluminium, Acta Metall. Mater. 43 (1995) 2001–2012, https://doi.org/10.1016/0956-7151(94)00405-7.
[32] Z. Liu, M. Rakita, X. Wang, W. Xu, Q. Han, situ formed Al3Ti particles in Al alloy matrix and their effects on the microstructure and mechanical properties of 7075 alloy, J. Mater. Res. 29 (2014) 1354–1361, https://doi.org/10.1557/JMR.2014.123.
[33] F. Wang, Z. Liu, D. Qiu, J.A. Taylor, M.A. Easton, M.X. Zhang, Revisiting the role of peritectics in grain refinement of Al alloys, Acta Mater. 61 (2013) 360–370, https://doi.org/10.1016/J.ACTAMAT.2012.09.075.
[34] D.H. St. John, L.M. Hogan, Metallography and growth crystallography of Al3Ti in Al-Ti alloys up to 5 wt% Ti, J. Cryst. Growth 46 (1979) 387–398, https://doi.org/10.1016/0022-0248(79)90087-3.
[35] F. Belelli, R. Casati, M. Vedani, J. Volpp, Design and characterization of Al–Mg–Si–Zr alloys with improved laser powder bed fusion processability, 2021 53:1, Metall. Mater. Trans. A 53 (2021) 331–343, https://doi.org/10.1007/S11661-021-06531-Y.
[36] S. Griffiths, M.D. Rossell, J. Croteau, N.Q. Vo, D.C. Dunand, C. Leinenbach, Effect of laser rescanning on the grain microstructure of a selective laser melted Al-Mg-Zr alloy, Mater. Charact. 143 (2018) 34–42, https://doi.org/10.1016/J.MATCHAR.2018.03.033.
[37] N. Iqbal, N.H. Van Dijk, S.E. Offerman, M.P. Moret, L. Katgerman, G.J. Kearley, Real-time observation of grain nucleation and growth during solidification of aluminium alloys, Acta Mater. 53 (2005) 2875–2880, https://doi.org/10.1016/J.ACTAMAT.2005.02.045.
[38] N. Iqbal, van, N.H. Dijk, T. Hansen, L. Katgerman, G.J. Kearley, The role of solute titanium and TiB2 particles in the liquid–solid phase transformation of aluminum alloys, Mater. Sci. Eng. A 386 (2004) 20–26, https://doi.org/10.1016/J.MSEA.2004.06.068.
[39] T.E. Quested, Understanding mechanisms of grain refinement of aluminium alloys by inoculation, Mater. Sci. Technol. 20 (2004) 1357–1369, https://doi.org/10.1179/026708304225022359.
[40] Z. Fan, Y. Wang, Y. Zhang, T. Qin, X.R. Zhou, G.E. Thompson, et al., Grain refining mechanism in the Al/Al–Ti–B system, Acta Mater. 84 (2015) 292–304, https://doi.org/10.1016/J.ACTAMAT.2014.10.055.
[41] J. Li, F.S. Hage, Q.M. Ramasse, P. Schumacher, The nucleation sequence of α-Al on TiB2 particles in Al-Cu alloys, Acta Mater. 206 (2021) 116652, https://doi.org/10.1016/J.ACTAMAT.2021.116652.
[42] X. Wang, J. Song, W. Vian, H. Ma, Q. Han, The interface of TiB2 and Al3Ti in molten aluminum, 2015 47:6, Metall. Mater. Trans. B 47 (2015) 3285–3290, https://doi.org/10.1007/S11663-015-0570-0.
[43] G. Sha, H. Möller, W.E. Stumpf, J.H. Xia, G. Govender, S.P. Ringer, Solute nanostructures and their strengthening effects in Al–7Si–0.6Mg alloy F357, Acta Mater. 60 (2012) 692–701, https://doi.org/10.1016/J.ACTAMAT.2011.10.029.
[44] J.H. Rao, Y. Zhang, K. Zhang, A. Huang, C.H.J. Davies, X. Wu, Multiple precipitation pathways in an Al-7Si-0.6Mg alloy fabricated by selective laser melting, Scr. Mater. 160 (2019) 66–69, https://doi.org/10.1016/J.SCRIPTAMAT.2018.09.045.
[45] Y. Wang, Y. Lu, J. Xu, S. Zhang, W. Wu, Z. Chen, The effects of Ti on the precipitation evolution and age-hardening behavior of Al–7Si–Mg alloy, Intermetallics 148 (2022) 107642, https://doi.org/10.1016/J.INTERMET.2022.107642.
[46] G.S. Wang, L. Geng, Microstructure formation mechanism of (Al2O3+TiB2+Al3Ti)/Al composites fabricated by reactive hot pressing, Key Eng. Mater. 353–358 (2007) 1439–1442, https://doi.org/10.4028/WWW.SCIENTIFIC.NET/KEM.353-358.1439.
[47] M. Belfi, G. Lupi, P. Martin, M. Santofimia, A. Gruttadauria, R. Casati, et al., Quenching & partitioning vs. direct tempering in powder bed fusion – laser beam AISI 420: impact on microstructural features and mechanical behavior, Mater. Sci. Eng. A 952 (2026) 149614, https://doi.org/10.1016/J.MSEA.2025.149614.
[48] I. Serrano-Munoz, A. Ulbricht, T. Fritsch, T. Mishurova, A. Kromm, M. Hofmann, et al., Scanning manufacturing parameters determining the residual stress state in LPBF IN718 small parts, Adv. Eng. Mater. 23 (2021) 2100158, https://doi.org/10.1002/adem.202100158.
[49] P. Van Cauwenbergh, V. Samaee, L. Thijs, J. Nejezchlebová, P. Sedlák, A. Iveković, et al., Unravelling the multi-scale structure–property relationship of laser powder bed fusion processed and heat-treated AlSi10Mg, Sci. Rep. 11 (2021), https://doi.org/10.1038/s41598-021-85047-2.
[50] A. Kumar Ramavajjala, T.R. Dandekar, R.K. Khatirkar, C. Joshi, R.N. Chouhan, A. Agnihotri, A review on the correlation between microstructure, heat treatment and mechanical properties of additively manufactured AlSi10Mg by LPBF, Crit. Rev. Solid State Mater. Sci. 50 (2025) 239–274, https://doi.org/10.1080/10408436.2024.2414012.
[51] C.S. Kim, K. Cho, M.H. Manjili, M. Nezafati, Mechanical performance of particulate-reinforced Al metal-matrix composites (MMCs) and Al metal-matrix nano-composites (MMNCs), J. Mater. Sci. 52 (2017) 13319–13349, https://doi.org/10.1007/S10853-017-1378-X/METRICS.